A simplified model for high-rate actuation of shape memory alloy torque tubes using induction heating

Robert N Saunders[1], James G Boyd[1], Darren J Hartl[1],
Frederick T Calkins[2] and Dimitris C Lagoudas[1]

Abstract

Shape memory alloy actuators deliver high forces while being compact and reliable, making them ideal for consideration in aerospace applications. Induction heating of shape memory alloy actuators, specifically tubes that twist about the longitudinal axis, has recently been studied experimentally and computationally using finite element analysis. Reduced-order models for the torsional behavior of shape memory alloy tubes and induction heating of general metallic tubes exist, and thus, it is possible for these thermal and mechanical models to be combined and numerically solved. This work develops and implements an engineering model for inductively heated shape memory alloy tubes based on the reduction of the governing partial differential equations in space and time to an ordinary differential equation in time. An example solution is compared to finite element analysis results and agrees well. Finally, the ordinary differential equation is linearized and solved analytically. The linearized model agrees well with the nonlinear ordinary differential equation and finite element model.

Introduction

Shape memory alloys (SMAs) are active materials that provide lightweight, compact actuation with a high volume–specific mechanical energy density. Actuation via SMAs is generally achieved using a thermal stimulus to affect the recovery of inelastic strains generated following the application of a mechanical stimulus. The mechanical loading transforms the SMA from the parent phase (austenite) to one or more crystallographic variants of martensite (Otsuka and Wayman, 1999), and the thermal stimulus is then used to generate recovery by way of a diffusionless solid-to-solid transformation back to austenite. Although there is only a single variant of austenite, there can be many variants of martensite (Boyd and Lagoudas, 1996). These martensite variants can be oriented under the appropriate application of stress and temperature, resulting in reconfigurable strains that can be recovered during martensitic transformation. This is known as the shape memory effect (SME) and provides a solid-state alternative in general actuation applications. Reliable SME must be "trained" in the SMA by thermomechanically cycling the actuator under load in the direction of desired actuation until a stable hysteresis is achieved. Based on

a number of factors, training may result in an SMA component that favors a particular internal distribution of oriented martensite variants that can generate and recover substantial deformations under no applied load. This behavior is known as the two-way SME. To provide an alternative to traditional wire-based SMA actuation solutions, recent developments have shown SMA torsional actuators, commonly torque tubes, that can be trained and implemented in large-scale aerospace actuation applications such as wing twisting (Hartl and Lagoudas, 2007; Herrington et al., 2015; Sanders et al., 2004; Saunders et al., 2014), rotor blade twisting (Kennedy et al., 2004; Prahlad and Chopra, 2001), and space-based radiator morphing (Bertagne et al., 2015a). Reliable methods to accurately characterize and model

[1]Department of Aerospace Engineering, Texas A&M University, College
Station, TX, USA
[2]Boeing Research & Technology, Seattle, WA, USA

Corresponding author:
James G Boyd, Department of Aerospace Engineering, Texas A&M
University, 741A HR Bright, 3141 TAMU, College Station, TX
77843-3141, USA.
Email: jgboyd@tamu.edu

the behavior of these torsional actuators under a variety of thermal and mechanical loading conditions have been studied by many authors (Keefe and Carman, 2000; Mabe et al., 2004, 2013; Mirzaeifar et al., 2010).

While SMAs have a very high volumetric energy density compared to other actuators, their actuation rate and frequency is limited by how quickly heat can be added to and removed from a metallic SMA component. Many authors suggest methods of heating and cooling, a summary of which can be found in Saunders et al. (2016). Of all of the heating methods described by these authors, perhaps the best option for large actuators such as torque tubes is induction heating. Induction heating requires less current to heat large pieces than resistive heating (generally accepted as the most efficient heating method) and is not rate limited by thermal conductivity as in conduction heating. Induction heating is a noncontact heating method whereby an alternating current is input to a coil, inducing a time-harmonic electromagnetic field surrounding the coil. An electrically conductive workpiece in the vicinity of the coil (and the field it generates) experiences an induced internal current at the same frequency as the exciting frequency but having an opposite flow of current. The induced currents, known as *eddy currents*, result in a localized Joule heating effect in the workpiece. Analytical and/or computational models of SMA components in an electromagnetic field are needed to understand how active materials and induction heating interact. Takagi et al. (2001) showed simulations of an electromagnetic field in an SMA plate using a phenomenological model. Saunders et al. (2016) developed a modeling framework applicable to any size or shape of SMA component. Both of these efforts utilized a finite element (FE) solution, which can become computationally expensive. To reduce this computational expense, some authors have developed analytical, semi-analytical, and reduced numerical solutions to SMA actuation problems (Bekker and Brinson, 1997; Brinson and Lammering, 1993; Lee and Mavroidis, 2002; Mirzaeifar et al., 2010; Tabesh et al., 2013) and induction heating (Davies and Simpson, 1979; Lupi et al., 2015). These non-FE solutions are especially useful for control of SMA actuators, where simplified plant models can be of great utility (Friedman et al., 2011).

The objective of this work is to develop reduced numerical and analytical solutions for the problem of an inductively heated SMA torque tube. This is accomplished by reducing the governing equations from partial differential equations in space and time to an ordinary differential equation (ODE) in time. This article is structured as follows: We first present the governing equations for linear momentum, thermodynamics, electromagnetics, and SMA constitutive behavior in their full forms. The problem is then reduced to a nonlinear ODE and then linearized so that it can be analytically solved. Finally, the results of the nonlinear ODE model and analytical solutions are compared to the results from FE models.

Governing equations

We assume small deformations so that the material time derivative d/dt can be replaced by the local time derivative $\partial/\partial t$, which is denoted by an overhead dot, that is, $(\dot{\ })$. We also denote the magnitude of a vector as $|\cdot|$, and the magnitude of a complex vector is given by $\sqrt{(\cdot)(\cdot)^*}$ where the $(*)$ denotes the complex conjugate of the vector. That is for a vector $x = a + bj$, the complex conjugate $x^* = a - bj$ and its magnitude $|x| = \sqrt{xx^*} = \sqrt{a^2 + b^2}$.

Physical principles

In static problems, the conservation of linear momentum requires universal local satisfaction of

$$\nabla \cdot \boldsymbol{\sigma} + \boldsymbol{f} = 0 \tag{1}$$

where $\boldsymbol{\sigma}$ is the (symmetric) Cauchy stress tensor. However, in this work, the electromagnetic (Tiersten, 1990) and gravitation body forces

$$\boldsymbol{f} = \rho^c \boldsymbol{E} + (\nabla \boldsymbol{E})\boldsymbol{P} + \boldsymbol{J} \times \boldsymbol{B} + (\boldsymbol{B}\nabla)^T \boldsymbol{M} + \rho^m \boldsymbol{g} \tag{2}$$

In these equations, ρ^c is the free electric charge density, $\boldsymbol{E}$ is the electric field intensity, $\boldsymbol{P}$ is the polarization, $\boldsymbol{J}$ is the current density, $\boldsymbol{B}$ is the magnetic flux density, $\boldsymbol{M}$ is the magnetization, ρ^m is the mass density, and $\boldsymbol{g}$ is the gravitational constant. The term $\boldsymbol{J} \times \boldsymbol{B}$ is the most significant. For this work, the maximum values of $\boldsymbol{J}$ and $\boldsymbol{B}$ are on the order of 14 MA/m^2 and 0.025 T, which results in a radial body force of approximately 0.35 MN/m^3 in the SMA tube. The associated stress is negligible compared to the stress due to applied torque so that $\nabla \cdot \boldsymbol{\sigma} = 0$. The linear strain–displacement equations (Bower, 2011) are used such that

$$\boldsymbol{\varepsilon} = \frac{1}{2}\left[\nabla \boldsymbol{u} + (\nabla \boldsymbol{u})^T\right] \tag{3}$$

where $\boldsymbol{\varepsilon}$ is the total strain tensor and $\boldsymbol{u}$ is the displacement vector. The first law of thermodynamics (Maugin, 2013) is written as

$$\rho^m \dot{u} = \boldsymbol{\sigma} : \dot{\boldsymbol{\varepsilon}} + \boldsymbol{E} \cdot \dot{\boldsymbol{D}} + \boldsymbol{H} \cdot \dot{\boldsymbol{B}} + \boldsymbol{E} \cdot \boldsymbol{J} - \nabla \cdot \boldsymbol{q} \tag{4}$$

where u is the specific internal energy, $\boldsymbol{H}$ is the magnetic field intensity, $\boldsymbol{D}$ is the electric displacement, and $\boldsymbol{q}$ is the conduction heat flux vector. In addition to the first law, the second law must be used to develop thermodynamically consistent constitutive equations. The second law can be written in the form of the Clausius–Planck inequality as

$$\rho^m \dot{s} + \nabla \cdot \boldsymbol{q} \geq 0 \tag{5}$$

where s is the entropy. Time varying electromagnetic fields such as those in induction heating are described by Maxwell's equations in the local form using a magneto-quasi-static approximation (frequencies below about $10^9\,$Hz, the rate of charge displacement, $\dot{D}$, is negligible compared to the conduction current; Rudnev et al., 2002; Sadiku, 2014; Westgard, 1996) as

$$\nabla \times \boldsymbol{H} = \boldsymbol{J} \quad \text{(Ampere's law)} \tag{6a}$$

$$\nabla \times \boldsymbol{E} = -\dot{\boldsymbol{B}} \quad \text{(Faraday's law)} \tag{6b}$$

$$\nabla \cdot \boldsymbol{B} = 0 \quad \text{(Gauss' law for magnetism)} \tag{6c}$$

The magneto-quasi-static approximation eliminates the need for Gauss' law ($\nabla \cdot \boldsymbol{D} = \rho^c$) in Maxwell's equations because it is no longer coupled to Ampere's law.

Three-dimensional constitutive and field equations

A Gibbs free energy is chosen to describe an arbitrary SMA body in an electromagnetic field with the following independent variables: $G = G(\boldsymbol{\sigma}, T, \boldsymbol{D}, \boldsymbol{B}, \boldsymbol{\varepsilon}^t, \xi, g^t)$, where T is the temperature, $\boldsymbol{\varepsilon}^t$ is the transformation strain tensor, ξ denotes the martensite volume fraction, and g^t is the transformation hardening energy. The Coleman–Noll procedure (Coleman and Noll, 1963, 1964) can be applied to derive

$$s = -\frac{\partial G}{\partial T} \tag{7a}$$

$$\boldsymbol{\varepsilon} = -\rho^m \frac{\partial G}{\partial \boldsymbol{\sigma}} \tag{7b}$$

$$\boldsymbol{E} = \rho^m \frac{\partial G}{\partial \boldsymbol{D}} \tag{7c}$$

$$\boldsymbol{H} = \rho^m \frac{\partial G}{\partial \boldsymbol{B}} \tag{7d}$$

Application of the second law of thermodynamics results in a dissipation inequality, which is assumed to be able to be decomposed into the following three inequalities

$$\boldsymbol{E} \cdot \boldsymbol{J} \geq 0 \tag{8a}$$

$$-\boldsymbol{q} \cdot \nabla T \geq 0 \tag{8b}$$

$$\frac{\partial G}{\partial \boldsymbol{\varepsilon}^t} : \dot{\boldsymbol{\varepsilon}}^t + \frac{\partial G}{\partial \xi} \dot{\xi} + \frac{\partial G}{\partial g^t} \dot{g}^t \geq 0 \tag{8c}$$

The first two inequalities are decoupled by neglecting thermoelectric effects (i.e. Seebeck and Peltier effects), and the third represents the generalized thermodynamical forces associated with transformation (Lagoudas, 2008; Lagoudas et al., 2012). The form of the free energy is chosen so that a magnetic constitutive relation, Ohm's law, and Fourier's law are given by

$$\boldsymbol{B} = \mu_0 \mu_r \boldsymbol{H} \tag{9a}$$

$$\boldsymbol{E} = \rho \boldsymbol{J} \tag{9b}$$

$$\boldsymbol{q} = -k\nabla T \tag{9c}$$

where k is the thermal conductivity.

There are many constitutive models that describe SMA behavior (Lagoudas et al., 2006; Patoor et al., 2006). The model chosen herein was developed by Lagoudas et al. (Boyd and Lagoudas, 1996; Lagoudas, 2008; Lagoudas et al., 2012). This model is computationally efficient and has been proven experimentally accurate under a variety of thermomechanical loading conditions (Hartl et al., 2011). The core model has been modified to account for plasticity (Hartl and Lagoudas, 2009) and transformation-induced anisotropy (Hartl et al., 2012, 2013).

Because the electromagnetic and thermomechanical terms in the free energy are assumed to be uncoupled, the thermomechanical-specific Gibbs free energy due to the austenite, martensite, and mixed phases is given by

$$G^{TM}(\boldsymbol{\sigma}, T, \boldsymbol{\varepsilon}^t, \xi, g^t) = G^A(\boldsymbol{\sigma}, T) +$$
$$\xi\big[G^M(\boldsymbol{\sigma}, T) - G^A(\boldsymbol{\sigma}, T)\big] + G^{mix}(\boldsymbol{\sigma}, \boldsymbol{\varepsilon}^t, g^t) \tag{10}$$

where G^A and G^M represent the Gibbs free energy in the austenite and martensite phases, respectively. Assuming a quadratic stress dependence, G^ζ for $\zeta = A, M$ gives

$$G^\zeta(\boldsymbol{\sigma}, T) = -\frac{1}{2\rho^m}\boldsymbol{\sigma} : \boldsymbol{S}^\zeta \boldsymbol{\sigma} - \frac{1}{\rho^m}\boldsymbol{\sigma} : \boldsymbol{\alpha}^\zeta(T - T_0) +$$
$$c^\zeta\left[(T - T_0) - T\ln\left(\frac{T}{T_0}\right)\right] - s_0^\zeta T + u_0^\zeta \tag{11}$$

and the mixing term is given as

$$G^{mix}(\boldsymbol{\sigma}, \boldsymbol{\varepsilon}^t, g^t) = -\frac{1}{\rho^m}\boldsymbol{\sigma} : \boldsymbol{\varepsilon}^t + \frac{1}{\rho^m}g^t \tag{12}$$

The parameters $\boldsymbol{S}$, T_0, s_0, and u_0 are the compliance tensor, reference temperature, specific reference entropy, and specific reference internal energy, respectively. The values of $\boldsymbol{S}$, s_0, and u_0 are all assumed to be dependent on the phase of the material. The specific heat c, density ρ^m, and the second-order coefficient of thermal expansion $\boldsymbol{\alpha}$ are assumed constant regardless of phase. The phase-dependent parameters are evaluated by a rule of mixtures in terms of ξ. For example, the compliance tensor $\boldsymbol{S}(\xi)$ is found as

$$\boldsymbol{S}(\xi) = \boldsymbol{S}^A + \xi\big(\boldsymbol{S}^M - \boldsymbol{S}^A\big) = \boldsymbol{S}^A + \xi\tilde{\boldsymbol{S}} \tag{13}$$

Now using the procedure of Coleman–Noll (equation (7)), the total strain and entropy are obtained as

$$\boldsymbol{\varepsilon} = -\rho^m\frac{\partial G^{TM}}{\partial \boldsymbol{\sigma}} = \boldsymbol{S}(\xi)\boldsymbol{\sigma} + \boldsymbol{\alpha}(\xi)(T - T_0) + \boldsymbol{\varepsilon}^t \tag{14}$$

and

$$s = -\frac{\partial G^{TM}}{\partial T} = \frac{1}{\rho^m}\boldsymbol{\sigma} : \boldsymbol{\alpha} + c\ln\left(\frac{T}{T_0}\right) + s_0 \qquad (15)$$

Equation (14) can be rewritten in a more common form as Hooke's law

$$\boldsymbol{\sigma} = \boldsymbol{S}^{-1}\varepsilon^{el} = \boldsymbol{S}^{-1}[\varepsilon - \varepsilon^t - \boldsymbol{\alpha}(T - T_0)] \qquad (16)$$

The evolution equations governing the transformation strain and hardening are given as

$$\dot{\varepsilon}^t = \dot{\xi}\boldsymbol{\Lambda}^t(\bar{\sigma}^{eff}) \qquad (17a)$$

$$\dot{g}^t = \left[f^t - \beta\boldsymbol{\Lambda}^t(\bar{\sigma}^{eff})\right]\dot{\xi} \qquad (17b)$$

$$\boldsymbol{\Lambda}^t(\bar{\sigma}^{eff}) = \begin{cases} \frac{3}{2}H^{cur}(\bar{\sigma}^{eff})\frac{s^{eff}}{\bar{\sigma}^{eff}}; & \dot{\xi}>0 \\ \frac{\varepsilon^{t-r}}{\xi^r}; & \dot{\xi}<0 \end{cases} \qquad (17c)$$

$$H^{cur}(\bar{\sigma}^{eff}) = H_{max}\left(1 - e^{-k^t\bar{\sigma}^{eff}}\right) \qquad (17d)$$

$$\boldsymbol{\sigma}^{eff} = (\boldsymbol{\sigma} + \boldsymbol{\beta}) \qquad (17e)$$

where H_{max} is the maximum uniaxial transformation strain, s^{eff} is the deviatoric effective stress, ε^{t-r} is the transformation strain tensor at cycle reversal, ξ^r is the martensitic volume fraction at cycle reversal, β is the back stress tensor developed during past training and which does not evolve, k^t is a parameter that controls the rate at which H^{cur} evolves exponentially, σ^{eff} is the Mises equivalent of the effective stress given as

$$\bar{\sigma}^{eff} = \sqrt{\frac{3}{2}s^{eff} : s^{eff}} \qquad (18)$$

and f^t is given for forward and reverse transformation as

$$f^t = \begin{cases} \frac{1}{2}a_1(1 + \xi^{n_1} - (1-\xi)^{n_2}) + a_3; & \dot{\xi}>0 \\ \frac{1}{2}a_2(1 + \xi^{n_3} - (1-\xi)^{n_4}) - a_3; & \dot{\xi}<0 \end{cases} \qquad (19)$$

A transformation function constraining the evolution of the martensitic volume fraction is postulated such that

$$\Phi^t = \begin{cases} \Phi^t_{fwd} = \Pi - Y^t; & \dot{\xi}>0 \\ \Phi^t_{rev} = -\Pi - Y^t; & \dot{\xi}<0 \end{cases} \qquad (20)$$

which is constrained in the manner of classical plasticity so that

$$\Phi^t \leq 0, \quad \dot{\xi}\Phi^t = 0, \quad 0 \leq \xi \leq 1 \qquad (21)$$

with the thermodynamic driving force Π given by

$$\Pi(\boldsymbol{\sigma}, T, \xi) = \boldsymbol{\Lambda}^t : \boldsymbol{\sigma}^{eff} + \frac{1}{2}\boldsymbol{\sigma} : \tilde{\boldsymbol{S}}\boldsymbol{\sigma} \\ + \rho^m\tilde{s}_0 T - \rho^m\tilde{u}_0 - f^t \qquad (22)$$

where $\tilde{s}_0$ and $\tilde{u}_0$ are the difference in reference entropy and internal energy, respectively, between austenite and martensite. The constant Y^t is a critical value at which transformation occurs; a_1, a_2, and a_3 are transformation hardening coefficients; and $n_1, \ldots, n_4$ are transformation hardening exponents. The parameters $\tilde{s}_0$, $\tilde{u}_0$, Y^t, a_1, a_2, and a_3 can all be expressed in terms of the phase diagram properties M_s, M_f, A_s, A_f, C^A, and C^M (Lagoudas et al., 2012).

The constitutive equations must be further manipulated to determine the effects of the latent heat of phase change. The first law of thermodynamics (equation (4)) is expanded via equation (7b) as

$$\rho^m\dot{u} = \boldsymbol{\sigma} : (\dot{\varepsilon}^{el} + \boldsymbol{\alpha}\dot{T} + \boldsymbol{\Lambda}\dot{\xi}) \\ + \boldsymbol{E}\cdot\boldsymbol{J} + \boldsymbol{E}\cdot\dot{\boldsymbol{D}} + \boldsymbol{H}\cdot\dot{\boldsymbol{B}} - \nabla\cdot\boldsymbol{q} \qquad (23)$$

A Legendre transformation is needed to combine and manipulate the Gibbs free energy and the first and second laws into more useful forms. This transformation is given by

$$\rho^m u = \rho^m G + \boldsymbol{\sigma} : \boldsymbol{\varepsilon} + \rho^m Ts \qquad (24)$$

Combining equations (23) and (24) gives

$$T\dot{s} = \frac{1}{\rho^m}\Pi\dot{\xi} + \boldsymbol{E}\cdot\boldsymbol{J} - \nabla\cdot\boldsymbol{q} \qquad (25)$$

In equation (25), $\dot{s}$ can be expanded by the definition of entropy to produce an equation that is a function of $\dot{T}$ and $\dot{\xi}$, where $\dot{\xi}$ can be written in terms of $\dot{T}$ (Boyd and Lagoudas, 1996). In the previous work of Saunders et al. (2016), the effects of thermomechanical coupling due to latent heat were not modeled in the finite element analysis (FEA) implementation. This shortcoming will be addressed in the this new reduced-order model.

Torque tube reduction

We assume that the torque tube SMA actuator is thin walled, axisymmetric, and that there are no end effects. The tube is shown schematically in Figure 1 with solenoid induction coil and induced magnetic field lines. The induced currents are spatially nonuniform, and their distribution depends on the workpiece shape, its electromagnetic properties, the eddy current frequency, the proximity of the workpiece to the coil, and the existence of other electrically conductive or magnetic bodies in the vicinity. The combination of these parameters affects the depth to which the magnetic field can penetrate the workpiece, known as the *skin effect*. The penetration depth δ is defined as the distance from the
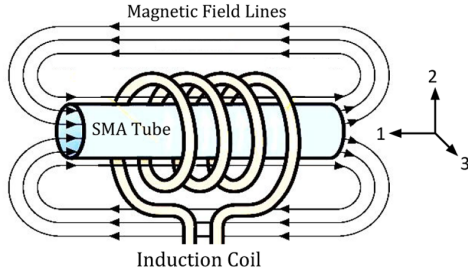
Figure 1. Thin-walled SMA tube schematic diagram with induction coil and induced magnetic field lines.

workpiece surface at which the magnetic field has decayed to a factor of e^{-1} relative to its surface value (Davies and Simpson, 1979) and is given by

$$\delta = \sqrt{\frac{\rho}{\pi \mu_0 \mu_r f}} \tag{26}$$

where ρ is the electrical resistivity, μ_0 is the magnetic permeability of vacuum $(4\pi \times 10^{-7}\,\text{H/m})$, μ_r is the relative magnetic permeability, and f is the frequency in hertz of the current. Results shown in Figure 6 are for an applied frequency equal to 55 kHz, for which the skin depth is 1.9 mm. The thickness of the torque tube is 1.9 mm, so we can assume that the Joule heating is distributed fairly uniformly through the thickness of the tube. A detailed FEA of the temperature distribution in a tube of thickness 1.95 mm was conducted by Saunders et al. (2016). Figures 14 and 15 of Saunders et al. (2016) indicate that for a frequency of 55 kHz, the temperature has a peak difference of 5°C between the inner and outer radii of a tube that is insulated on the outer radius and has natural convection with water on the inner radius, and the martensite volume fraction differs by 18% between the inner and outer radii. Higher (lower) frequencies have more (less) spatial variation in temperature and martensite volume fraction.

Reduced electromagnetic equations

There are two methods of determining electromagnetic power induced in the cylinder. The first reduces Maxwell's equations to a function of only the radial coordinate and then assumes that the radial variation is small. The second method begins by assuming the tube is thin walled and then developing the induced power based on the the flux induced in the thin-walled cylinder. Both solutions will be presented and then compared.

Method I: Maxwell's equation reduction. To begin the reduction of Maxwell's equations, recall the magneto-quasi-static approximation of Ampere's law with Ohm's law substituted (Lupi et al., 2015)

$$\nabla \times \boldsymbol{H} = \nabla \times \left(\frac{1}{\rho} \boldsymbol{E}\right) \tag{27}$$

which can be rewritten as

$$\nabla(\nabla \cdot \boldsymbol{H}) - \nabla^2 \boldsymbol{H} = \frac{1}{\rho} \nabla \times \boldsymbol{E} + \left(\nabla \frac{1}{\rho}\right) \times \boldsymbol{E} \tag{28}$$

Combining Gauss' law for magnetism with equation (9a) yields $\nabla \cdot \boldsymbol{H} = 0$. A similar process can be used with Faraday's law to yield $\nabla \times \boldsymbol{E} = -\mu_0 \mu_r \dot{\boldsymbol{H}}$. These relations with the assumption of a homogeneous permeability and resistivity yield

$$\nabla^2 \boldsymbol{H} = \frac{\mu_0 \mu_r}{\rho} \dot{\boldsymbol{H}} \tag{29}$$

As is common in induction heating, the excitation is considered to be sinusoidal giving $\boldsymbol{H} = \boldsymbol{H}_0 e^{j\omega t}$ and $\dot{\boldsymbol{H}} = j\omega \boldsymbol{H}$, where $\boldsymbol{H}_0$ contains the magnitude and phase angle of $\boldsymbol{H}$. This assumption allows equation (29) to be written as

$$\nabla^2 \boldsymbol{H}_0 = j\frac{\omega \mu_0 \mu_r}{\rho} \boldsymbol{H}_0 \tag{30}$$

Equation (30) can now be reduced to the case of a cylindrical workpiece by noting that $\boldsymbol{H}$ has only one nonzero component, directed along the longitudinal axis of the cylinder, and $\boldsymbol{E}$ has only one nonzero component, tangential to the circumference of the cylinder, which reduces the Laplacian of equation (30) to only a function of the radial direction r as given by

$$\nabla^2 = \frac{1}{r}\frac{\partial}{\partial r}\left(r\frac{\partial}{\partial r}\right) \tag{31}$$

and gives

$$\frac{\partial^2 H_0}{\partial r^2} + \frac{1}{r}\frac{\partial H_0}{\partial r} - j\frac{\omega \mu_0 \mu_r}{\rho} H_0 = 0 \tag{32}$$

Equation (32), after some manipulation, represents a Bessel differential equation of zero order with general solutions for H_0 and E_0 given by

$$H_0 = C_1 K_0\left(\sqrt{-j}m_r\right) + C_2 Y_0\left(\sqrt{-j}m_r\right) \tag{33a}$$

$$E_0 = \sqrt{-2j}\,\frac{\rho}{\delta}\left[C_1 K_1\left(\sqrt{j}m_r\right) + C_2 Y_1\left(\sqrt{j}m_r\right)\right] \tag{33b}$$

where C_1 and C_2 are constants to be determined, K_0 and Y_0 are zero-order Bessel functions of the first and second kind, K_1 and Y_1 are order 1 modified Bessel functions of the first and second kind, and $m_r(r) = \sqrt{2}r/\delta$. The Bessel functions are implemented in MATLAB where the ODE is also implemented and are not explicitly written here. For the problem of a hollow tube with inner radius r_i and outer radius r_e, the boundary conditions needed to solve for C_1 and C_2 are given by

$$H_0 = \begin{cases} H_{e0} = nI; & r = r_e \\ H_{i0}; & r = r_i \end{cases} \quad (34)$$

where H_{e0} is derived by assuming a long thin wire forms an infinite length solenoid around the tube giving an idealized version of Ampere's law with n being the turns per unit length and I is the peak current input to the coil. Solving for C_1 and C_2 then substituting into equation (33) gives

$$H_0 = H_{e0} \frac{F_{00}(m_i, m_r)}{F_{00}(m_i, m_e)} - H_{i0} \frac{F_{00}(m_e, m_r)}{F_{00}(m_i, m_e)} \quad (35a)$$

$$E_0 = \sqrt{-2j}$$
$$\frac{\rho}{\delta} \left[H_{e0} \frac{F_{01}(m_i, m_r)}{F_{00}(m_i, m_e)} - H_{i0} \frac{F_{01}(m_e, m_r)}{F_{00}(m_i, m_e)} \right] \quad (35b)$$

where the functions F_{00} and F_{01} are given by

$$F_{00}(x, y) = K_0\left(\sqrt{-j}y\right) Y_0\left(\sqrt{-j}x\right)$$
$$- K_0\left(\sqrt{-j}x\right) Y_0\left(\sqrt{-j}y\right) \quad (36a)$$

$$F_{01}(x, y) = K_1\left(\sqrt{-j}y\right) Y_0\left(\sqrt{-j}x\right)$$
$$- K_0\left(\sqrt{-j}x\right) Y_1\left(\sqrt{-j}y\right) \quad (36b)$$

and x and y are used as placeholders to indicate function inputs. The variables m_i and m_e correspond to $m_r(r)$ evaluated at $r = r_i$ and $r = r_e$, respectively.

To determine the radial distribution of H_0 and E_0, H_{i0} must be determined. The electromotive force (*emf*) induced in a coil of wire is linked to the change in magnetic field by Faraday's law. This can be applied at the inner surface of the tube to obtain

$$\oint E_{i0} dl = -A_i \mu_0 \dot{H}_{i0} \quad (37)$$

where $A_i = \pi r_i^2$ is the area enclosed by the inner surface of the tube and $\oint E_{i0} dl$ can be evaluated as $2\pi r_i E_{i0}$. Note that the permeability used is not the relative permeability because the previous equation is derived in the internal portion of the tube where there is no material, only air or vacuum. Recall that the magnetic field has been assumed sinusoidal giving $\dot{H}_{i0} = j\omega H_{i0}$. Solving equation (37) for E_{i0} and setting this equal to equation (36a) evaluated at r_i gives

$$-\frac{j\omega \mu_0 r_i}{2} H_{i0} = \sqrt{-2j} \frac{\rho}{\delta}$$
$$\left[nI \frac{F_{01}(m_i, m_i)}{F_{00}(m_i, m_e)} - H_{i0} \frac{F_{01}(m_e, m_i)}{F_{00}(m_i, m_e)} \right] \quad (38)$$

from which H_{i0} can be determined to be

$$H_{i0} = \frac{\sqrt{-2j} \frac{\rho nI}{\delta} \frac{F_{01}(m_i, m_i)}{F_{00}(m_i, m_e)}}{\sqrt{-2j} \frac{\rho}{\delta} \frac{F_{01}(m_e, m_i)}{F_{00}(m_i, m_e)} - \frac{j\omega \mu_0 r_i}{2}} \quad (39)$$

With H_{i0} known, E_0 can be determined and then currents in the body can be found by application of Ohm's law. Note that the determined E_0 is only valid in the workpiece where there is no source current applied; thus, the current found from application of Ohm's law will be the eddy current. The application of Poynting's vector allows for the time-averaged power derived using the Maxwell equation reduction Q_{ME} to be found (Lupi et al., 2015) as

$$Q_{ME} = \mathbf{E} \cdot \mathbf{J} = \frac{\rho}{2} J_{e0} \cdot J_{e0}^* \quad (40)$$

where J_{e0} is the eddy current density (A/m^2). Examining the previous equations, it can be seen that the power is a function of radius. The time-averaged power as a function of radius has a distribution close to that of an exponential function. We can apply the thin-walled tube assumption to this and examine a small segment through the thickness where the power will be approximately linear. To further reduce this variation from linear to constant, we take the mean value $\langle Q_{ME} \rangle$ to be

$$\langle Q_{ME} \rangle = \frac{1}{r_e - r_i} \int_{r_i}^{r_e} Q_{ME} \, dr \quad (41)$$

The normalized power $Q_{ME}/\langle Q_{ME} \rangle$ as a function of the normalized radius (0 at r_i, 1 at r_e) is shown in Figure 2. Note that the areas under the two curves are equal.

Method II: induced flux method. The previous method assumed that the tube was thin walled after
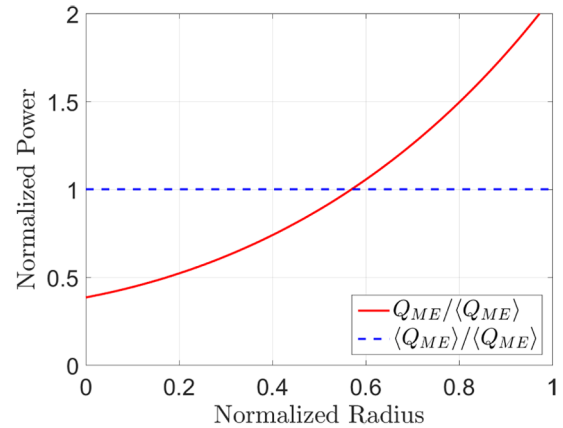

Figure 2. The normalized power $Q_{ME}/\langle Q_{ME} \rangle$ as a function of the normalized radius (0 at r_i, 1 at r_e).

determining the power in the cylinder as a function of radius (Davies and Simpson, 1979). An alternate derivation based on the assumption of a thin-walled tube is now presented. Since the cylinder is thin, the flux can be assumed constant through the thickness. Similar to equation (37), the emf e in the cylinder can be related to the magnetic field by

$$e = A\mu_0 \dot{H}_0^{ind} = jA\mu_0\omega H_0^{ind} \quad (42)$$

where A is total area enclosed by the cylinder (because $r_e \approx r_i$, $A \approx A_i$) and H_0^{ind} is the magnetic field induced in the cylinder. The process derived in Davies and Simpson (1979) assumes the material is nonmagnetic, which is true of the SMA materials considered ($\mu_r = 1$). Ohm's law can be used to relate the current I^{ind} to the emf e and resistance R of the cylinder given as

$$I^{ind} = \frac{e}{R} = j\frac{A\mu_0\omega}{\rho\pi d/(tl)}H_0^{ind} \quad (43)$$

where d, t, and l are the mean diameter, thickness, and length of the cylinder. Because the cylinder is thin, the induced magnetic field can be assumed to be decomposed into the applied magnetic field H_0^{app} less the field due to I^{ind} as

$$H_0^{app} = \frac{I^{ind}}{l} + H_0^{ind} = j\frac{At\mu_0\omega}{\rho\pi d}H_0^{ind} + H_0^{ind} \quad (44)$$

For simplification, let us introduce the constant

$$\Gamma = \frac{At\mu_0\omega}{\rho\pi d} = \frac{At}{\pi d}\frac{2}{\delta^2} = \frac{td}{2\delta^2} \quad (45)$$

which gives

$$H_0^{app} = (1 + j\Gamma)H_0^{ind} \quad (46)$$

The power derived using the induced flux method Q_{IF} in the cylinder can now be found as

$$Q_{IF} = eI^{ind} = \frac{e^2}{R} = \pi f\mu_0(Al)\frac{\Gamma}{1 + \Gamma^2}\left(H_0^{app}\right)^2 \quad (47)$$

where $H_0^{app} = nI$. Finally

$$Q_{IF} = \pi f\mu_0\left(\frac{Al}{V}\right)\frac{\Gamma}{1 + \Gamma^2}(nI)^2 \quad (48)$$

Note that Q_{IF} is divided by the volume of the cylinder to achieve the correct units of Watt/cubic meter.

Method comparison. To compare the two methods, we note that most applications of SMA torque tubes actually utilize a thick-walled tube ($d/t \leq 10$) rather than a thin-walled tube ($d/t \geq 10$). Here, we examine an 8-in (203-mm)-long SMA tube with outer diameter of 0.375 in (9.525 mm) and a variable wall thickness from
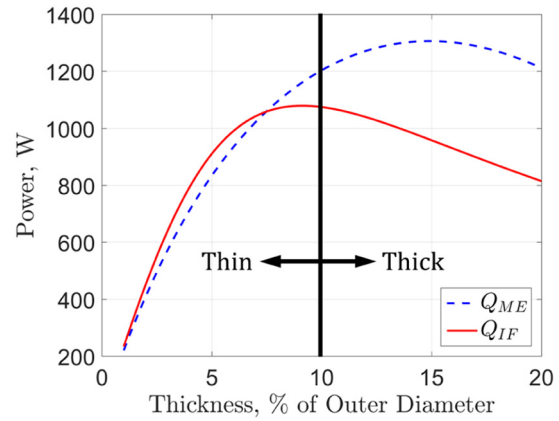

Figure 3. Comparison of Q_{ME} and Q_{IF} as a function of wall thickness.

1% to 20%, subject to induction heating using a 120 turn coil with peak current $I = 47$ A at $f = 49$ kHz. The results of a varying thickness are shown in Figure 3.

We see that Q_{IF} as obtained by equation (48) experiences a significant change as d/t approaches 10. Davies and Simpson (1979) notes that the developed solution is reasonably accurate for $d/t \geq 10$ and $t/\delta \leq 0.2$. Therefore, when a thickness is near or above 10%, as is the case with most common SMA torque tube actuators, Q_{ME} as obtained by equation (40) is likely a more accurate estimate. This assumption is based on the fact that Q_{IF} was developed to be accurate in a very specific range of tube thicknesses, and Q_{ME} was developed to model any size tube using a much more rigorous physical approach. Once outside of the range of thicknesses that Q_{IF} was developed for, the accuracy is significantly reduced due to the assumption of a constant through-thickness flux. Note that as the tube become thinner, the solutions converge to approximately the same value. As an additional point of comparison, the power given by Q_{ME} and Q_{IF} is 1204 and 1075 W, respectively, at a thickness of 10% of the diameter.

Reduced thermomechanical equations

As mentioned previously, prior FEA work excluded latent heat due to phase transformation and also excluded the phase and temperature dependence of the resistivity. These important effects are incorporated herein in to the novel ODE approach. The material constants in constitutive equations are best obtained from experiments in which the stress and strain are homogeneous, that is, do not vary spatially. However, in the case of the torque tube, the shearing stress in the elastic case varies linearly in the radial direction. Furthermore, the material constants are not determined from direct measurements of stress and strain, but rather from the applied torque and the angle of rotation, which are properties of the entire body, not a

material point. Therefore, one must choose a radius at which to assign the material constants, which are obtained by curve-fitting to the torque–rotation response. As long as the stress distribution is constant, any radial location can be used. During transformation, the stress distribution changes and does deviate from linearity, but as shown in Figure 16 of Saunders et al., 2016, the deviation is small. In the present case, we choose the outer radius because that is a location for which instruments can more easily be attached in subsequent studies. For a tube undergoing pure torsion, the three-dimensional (3D) stress state can be reduced to $\sigma_{23} = \sigma_{32} = \tau$, and all other components are null. The shear stress τ at the outer diameter d_e can be estimated by

$$\tau = \frac{T_r d_e}{\frac{1}{32}\pi\left(d_e^4 - d_i^4\right)} \tag{49}$$

where T_r is the torque and d_i is the inner diameters of the tube. The SMA model is simplified by considering the reduced stress state in a thin-walled tube under torsion and assuming that the stress is time independent, that is, a constant value during heating and cooling. A Gibbs free energy that is identical to the free energy formulated in equations (10) to (12) is used with the exception the thermoelastic term, which does not contribute to the shear stress, is neglected. This gives a total engineering shear strain γ and entropy as

$$\gamma = \mu(\xi)\tau + \gamma^t \tag{50a}$$

$$s = c\ln\left(\frac{T}{T_0}\right) + s_0 \tag{50b}$$

where μ is the shear modulus. The evolution equations (equation (17)) are reduced to

$$\dot{\gamma}^t = \dot{\xi}\Lambda^t(\tau) \tag{51a}$$

$$\dot{g}^t = \left[f^t - \beta\Lambda^t(\tau)\right]\dot{\xi} \tag{51b}$$

$$\Lambda^t(\tau) = \frac{\sqrt{3}}{2}H^{cur}(\tau) \tag{51c}$$

$$H^{cur}(\tau) = 2H_{max}\left(1 - e^{-\sqrt{3}k^t(\tau + \beta)}\right) \tag{51d}$$

where β is the two to three components of back stress with all other components being zero. The factor of 2 in equation (51d) has been added to make $H^{cur}(\tau)$ compatible with the engineering shear strain. In this formulation of the evolution equations, it is assumed that the tube is initially 100% martensite. Therefore, there is no need for $\Lambda^t(\tau)$ to have a different forward and reverse formulations. The thermodynamic driving force Π given by equation (22) is reduced so that

$$\Pi(\tau, T, \xi) = 2(\tau + \beta)\Lambda^t(\tau) + 2\tau^2\left(\frac{1}{\mu^M} - \frac{1}{\mu^A}\right)$$
$$+ \rho^m\tilde{s}_0 T - \rho^m\tilde{u}_0 - f^t \tag{52}$$

The transformation function constraining the evolution of the martensitic volume fraction (equation (20)) can be written as

$$\Phi^t = \begin{cases} \Phi_{fwd}^t = 2(1-D)(\tau + \beta)\Lambda^t(\tau) \\[4pt] \quad + 2\tau^2\left(\frac{1}{\mu^M} - \frac{1}{\mu^A}\right) + \rho^m\tilde{s}_0 T \quad;\dot{\xi}>0 \\[4pt] \quad -\rho^m\tilde{u}_0 - f_{fwd}^t - Y_0 \\[6pt] \Phi_{rev}^t = -2(1+D)(\tau + \beta)\Lambda^t(\tau) \\[4pt] \quad -2\tau^2\left(\frac{1}{\mu^M} - \frac{1}{\mu^A}\right) - \rho^m\tilde{s}_0 T \quad;\dot{\xi}<0 \\[4pt] \quad + \rho^m\tilde{u}_0 + f_{rev}^t - Y_0 \end{cases} \tag{53}$$

where D is a model parameter that captures the stress dependency of the critical thermodynamical force corresponding to the distinct forward and reverse transformation slopes on the phase diagram (Lagoudas et al., 2012). The parameters $\tilde{u}_0$, Y_0, a_1, a_2, and a_3 can be found as

$$a_1 = \rho^m\tilde{s}_0\left(M_f - M_s\right) \tag{54a}$$

$$a_2 = \rho^m\tilde{s}_0\left(A_s - A_f\right) \tag{54b}$$

$$a_3 = -\frac{a_1}{4}\left(1 + \frac{1}{n_1 + 1} - \frac{1}{n_2 + 1}\right)$$
$$+ \frac{a_2}{4}\left(1 + \frac{1}{n_3 + 1} - \frac{1}{n_4 + 1}\right) \tag{54c}$$

$$\rho^m\tilde{u}_0 = \frac{\rho^m\tilde{s}_0}{2}\left(M_s + A_f\right) + 2\beta\Lambda^t(0) \tag{54d}$$

$$Y_0 = \frac{\rho^m\tilde{s}_0}{2}\left(M_s - A_f\right) - a_3 - 2\beta D\Lambda^t(0) \tag{54e}$$

with

$$D = \frac{C_m - C_a}{(C_a + C_m)\left(\Lambda^t(\tau^*) + (\tau^* + \beta)\frac{\partial\Lambda^t(\tau^*)}{\partial\tau}\right)} \times$$
$$\left[\Lambda^t(\tau^*) + (\tau^* + \beta)\frac{\partial\Lambda^t(\tau^*)}{\partial\tau} + 2\tau^*\left(\frac{1}{\mu^M} - \frac{1}{\mu^A}\right)\right] \tag{55}$$

and

$$\rho^m\tilde{s}_0 = -\frac{4C_a C_m}{C_a + C_m}$$
$$\left[\Lambda^t(\tau^*) + (\tau^* + \beta)\frac{\partial\Lambda^t(\tau^*)}{\partial\tau} + 2\tau^*\left(\frac{1}{\mu^M} - \frac{1}{\mu^A}\right)\right] \tag{56}$$

where τ^* is the calibration shear stress at which the slopes of C_a and C_m are measured. With this

transformation function for the SMA tube under pure torsion known, equations (25) and (50b) can be combined to yield

$$\frac{1}{2}\rho J_{e0} \cdot J_{e0}^* - \nabla \cdot q = (-\Pi(\tau, T, \xi) + \rho^m \tilde{s}_0 T)\dot{\xi} + \rho^m c \dot{T} \tag{57}$$

Note that $(1/2)\rho J_{e0} \cdot J_{e0}^*$ gives the heating power due to induction. This term can be equivalently replaced by either Q_{ME} or Q_{IF}. In this work, as alluded to in the method comparison, we choose Q_{ME}. The shear stress rate $\dot{\tau}$ has also been neglected since it is assumed in this ODE that τ is time independent (i.e. the applied torque is constant). The eddy current density J_{e0} has only one component, the circumferential. Equation (57) can be rewritten by noting that $\dot{\xi}$ is only nonzero when the SMA is transforming and by recalling that $\dot{\xi}\Phi^t = 0$, giving

$$Q_{ME} - \nabla \cdot \boldsymbol{q} = (\mp Y^t + \rho^m \tilde{s}_0 T)\dot{\xi} + \rho^m c \dot{T} \tag{58}$$

where $Y^t = Y_0 + 2(\tau + \beta)D\Lambda^t(\tau)$ and the notation of "$\mp$" has been introduced with the upper sign used to indicate forward transformation and the lower to indicate reverse. Finally, it is noted that the only heat sources and sinks are due to induction heating and convective terms such that equation (58) can be written in its final form as

$$Q_{ME} - h\frac{A}{V}(T - T_\infty) = (\mp Y^t + \rho^m \tilde{s}_0 T)\dot{\xi} + \rho^m c \dot{T} \tag{59}$$

where h is the convection coefficient inside of the tube and A and V are the area and volume of the SMA tube, respectively. If latent heat effects are not considered in the ODE, the equation is linear.

Energy balance ODE implementation

The energy balance ODE (equation (59)) is implemented in MATAB using the return mapping algorithm as described in Qidwai et al. (2008). The inputs to this model are the initial temperature, SMA tube dimensions, electric current, frequency, number of coil turns, and the heating/cooling times. The ODE approach uses the Gauss–Seidel time marching scheme shown in Figure 4. This process has been successfully used in other coupled SMA-based problems (Bertagne et al., 2015b; Oehler, 2012). In this scheme, the appropriate initial conditions are passed to both the electromagnetic and thermomechanical algorithms. The thermomechanical problem is then solved for the first increment to obtain the current temperature and phase. The temperature and phase are then given to the electromagnetic problem to determine and evolve the electrical resistivity at the current step. This allows for a new Joule heating power to be determined. The heating
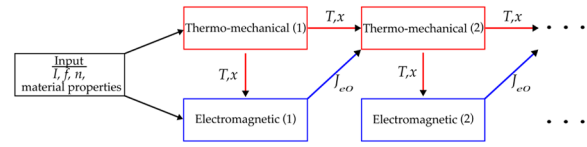

Figure 4. Gauss–Seidel time marching scheme used to couple the electromagnetic behavior to the thermomechanical behavior in the ODE approach.

power is then given back to the thermal problem, along with the previous temperature and phase, to determine a new temperature and phase. The process is continued in this manner for the duration of the heating and cooling process.

Analytical solution to linearized ODE

We linearized equation (59) to derive an analytical solution which approximately accounts for the effects of latent heat. We first recognize that $\dot{\xi}$ can be rewritten (Boyd and Lagoudas, 1996) as

$$\dot{\xi} = \left(-\frac{\partial \Pi}{\partial \xi}\right)^{-1} \left(\frac{\partial \Pi}{\partial \boldsymbol{\sigma}}\dot{\boldsymbol{\sigma}} + \frac{\partial \Pi}{\partial T}\dot{T}\right) \tag{60}$$

but restrict ourselves to $\dot{\sigma} \cong 0$, which gives

$$\dot{\xi} = \left(-\frac{\partial \Pi}{\partial \xi}\right)^{-1} \frac{\partial \Pi}{\partial T}\dot{T} \tag{61}$$

where $\partial \Pi/\partial T = \rho^m \tilde{s}_0$ and $\partial \Pi/\partial \xi = -\partial f^t/\partial \xi = -(f^t)$. Note that f^t as used in this work is nonlinear (known as the "smooth" hardening model developed by Lagoudas et al., 2012). To linearize this, we assume $n_i = 1$ and reduce f^t to the quadratic hardening model of Boyd and Lagoudas (1996) given as (Lagoudas et al., 2012)

$$f^t = \begin{cases} a_1\xi - \dfrac{a_2 + a_1}{4}; \dot{\xi} > 0 \\ a_2\xi + \dfrac{a_2 - a_1}{4}; \dot{\xi} < 0 \end{cases} \tag{62}$$

Now $\partial \Pi/\partial \xi$ can be found to be

$$-(f^t) = \begin{cases} -a_1; \dot{\xi} > 0 \\ -a_2; \dot{\xi} < 0 \end{cases} \tag{63}$$

which is no longer dependent on ξ. Equation (59) can be rewritten using equation (61) as

$$Q_{ME} - h\frac{A}{V}(T - T_\infty) = \left[(\mp Y^t + \rho^m \tilde{s}_0 T_f)\frac{\rho^m \tilde{s}_0}{(f^t)} + \rho^m c\right]\dot{T} \tag{64}$$

where T_f is the fixed temperature chosen to linearize the equation. As is done in typical lumped capacity models,
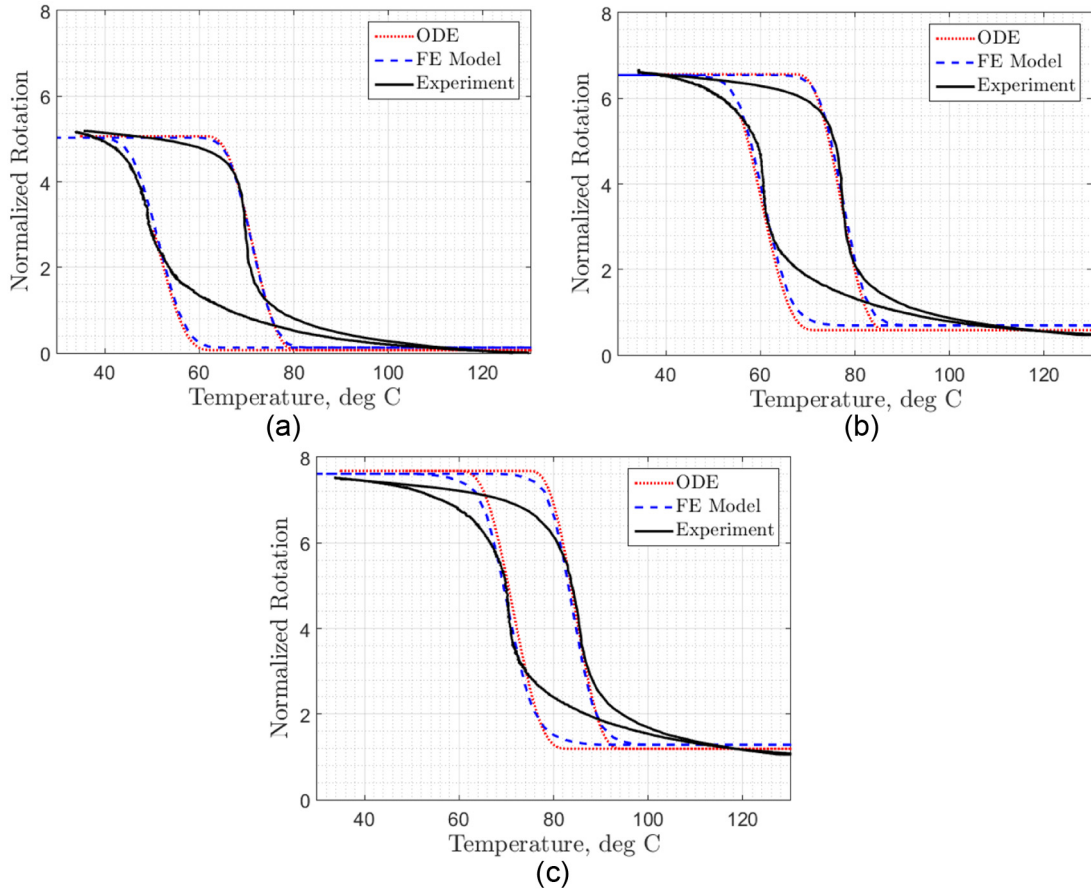
Figure 5. SMA calibration experiment compared to the ODE and calibrated FE model. The normalized rotation is the rotation measured multiplied by the ratio $d_e/(2L)$: (a) 10 MPa, (b) 70 MPa, and (c) 140 MPa.

we let $\theta = T - T_\infty$ such that $\dot{\theta} = \dot{T}$. We can now rearrange to obtain

$$\dot{\theta} = c_1\theta + c_2 \qquad (65)$$

where $c_1 = (h/c_3)(A/V)$ and $c_2 = (\rho/2c_3)J_{e0} \cdot J_{e0}^*$ with

$$c_3 = \begin{cases} \left(-Y^t + \rho^m\tilde{s}_0 T_f\right)\dfrac{\rho^m\tilde{s}_0}{a_1} + \rho^m c; & \dot{\xi}>0 \\[2mm] \left(Y^t + \rho^m\tilde{s}_0 T_f\right)\dfrac{\rho^m\tilde{s}_0}{a_2} + \rho^m c; & \dot{\xi}<0 \end{cases}$$

Equation (65) has the general solution

$$\theta = c_4 e^{-c_1 t} + \frac{c_2}{c_1} \qquad (66)$$

subject to initial conditions $\theta(0) = \theta_0 = T_0 - T_\infty$. Solving c_4 yields the form

$$\theta = \left(\theta_0 - \frac{c_2}{c_1}\right)e^{-t/c_1} + \frac{c_2}{c_1} \qquad (67)$$

A nondimensional form of equation (67) can be created by defining the normalized time $\mathfrak{T} = t/c_1$ and normalized temperature $\Theta = \theta/\theta_0$ and then dividing by θ_0 throughout, yielding

$$\Theta = (1 - \Theta^c)e^{-\mathfrak{T}} + \Theta^c \qquad (68)$$

where $\Theta^c = c_2/c_1\theta_0$.

Results

The remainder of this work will focus on induction heating of a homogeneous, prismatic SMA torque tube actuator with active length L of 8 in (203 mm), with outer and inner diameters d_e and d_i of 0.375 in (9.525 mm) and 0.225 in (5.715 mm), respectively. In all cases, the tube has a constant applied twisting moment on one end and is fixed at the other. The ODE constitutive parameters must be calibrated, and the results associated with this calibration are shown in Figure 5 and Table 1. To calibrate the constitutive model, an SMA torque tube is subjected to five constant torsional loads, three of which are shown, and the actuation response due to a changing temperature is measured. The temperature measured is the input to the FE model modeling a finite thickness tube and to

Table 1. SMA electromagnetic and mechanical constitutive material parameters (Saunders et al., 2016).

Property	Tube
Electromagnetic parameters	
μ_r	1.002
ρ_a ($\mu\Omega$ cm)	76
ρ_m ($\mu\Omega$ cm)	82
Heat transfer parameters	
γ (kg/m^3)	6450
c (J/kg/K)	850
k (W/m/K)	10
Thermoelastic parameters	
μ^A (GPa)	10.52[a]
μ^M (GPa)	6.58[a]
$\alpha_m = \alpha_a$ (/K)	0.00
Phase diagram parameters	
M_s, M_f (K)	335, 311
A_s, A_f (K)	333, 354
C_m, C_a (MPa/K)	5.5, 7.9
Transformation parameters	
H_{max} (%)	3.35
k^t (/MPa)	0.0172
β (MPa)	58
Smooth hardening parameters	
$n_{1,2,3,4}$	0.3

SMA: shape memory alloy.
[a]Calibrated from torsion testing.

the ODE simulating a thin-walled tube. The constitutive parameters are varied until the appropriate actuation response is achieved. For further details of the calibration, the interested reader is referred to Saunders et al. (2016).

Power variation

In the first study, the input power to the system is varied, and the temperature at the middle of the tube on the outer surface is examined. At this location, there are neither end effects nor variation tangentially around the tube. The power is varied by maintaining a constant induction frequency and varying the coil current across three discrete root mean square (RMS) levels: 49.9, 45.3, and 21.4 A at a frequency of 55 kHz; this corresponds to input power levels of 1150, 840, and 225 W, respectively. The parameters chosen for this study are based on the current experimental capabilities. Much higher heating rates are possible and able to be simulated with the models. Future optimization and improvement of the induction system will show more rapid heating times. The study models a 10-AWG copper magnet wire wrapped tightly around the SMA tube. No active cooling is considered, minimizing
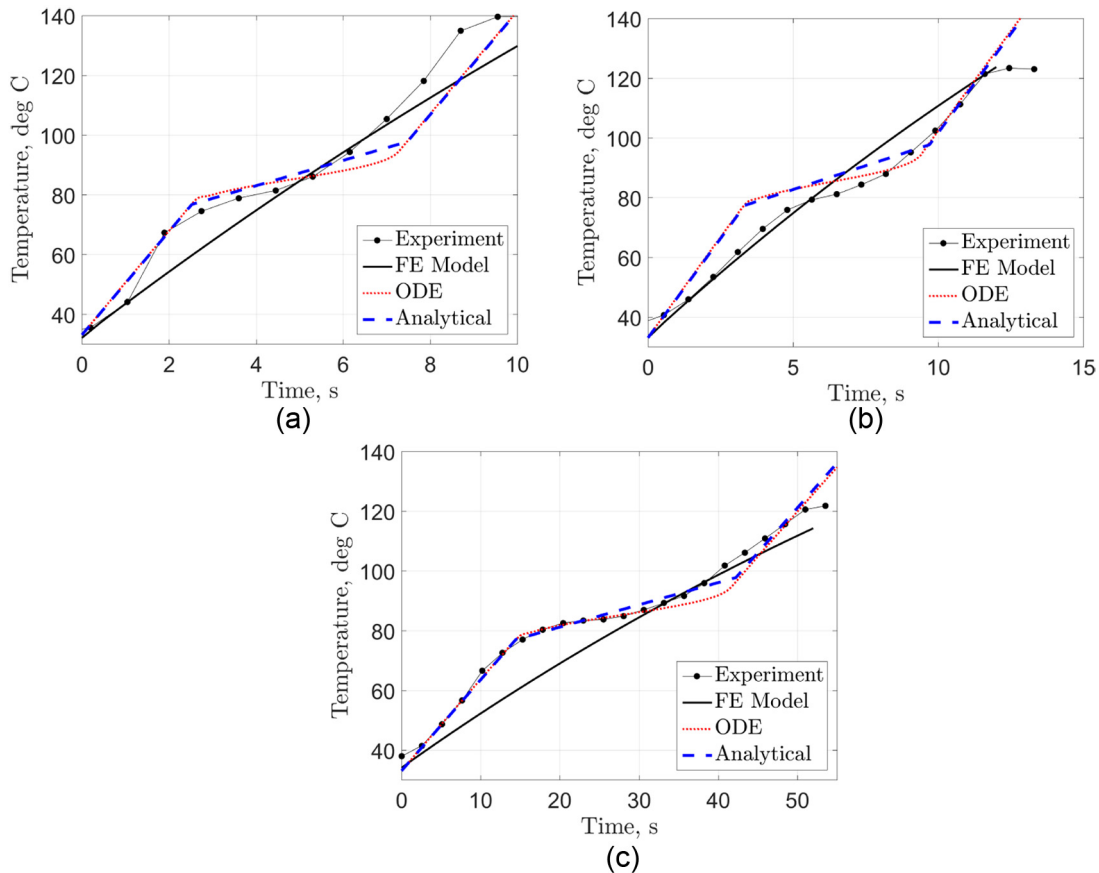

Figure 6. Power measurement study results. The highest heating rates correspond to the highest input power. (a) 1150 W induction heating power measurement, (b) 840 W induction heating power measurement, and (c) 225 W induction heating power measurement.

the number of possible variables in the numerical study. Thus, only the heating of the tube is modeled since cooling is accomplished by free convection over a long time relative to heating. The torque in all three power variations was held constant at 21 N m.

The results of the models are shown in Figure 6. The addition of the effects of latent heat in the nonlinear ODE (equations (40) and (59)) and analytical solutions (equation (67)) allows for the significant deviations from linearity to be captured, but in general, both solutions slightly overestimate the rate of heating in the SMA body relative to the FE model. The analytical solution agrees well with the nonlinear ODE with the only differences coming from the difference in transformation function. The ODE approach numerically solves a smooth hardening function where the analytical uses a quadratic hardening function. Differences in predicted temperature are relatively small when compared to the 83% average decrease in computation time when using the analytical solution versus the nonlinear ODE approach and 99% decrease in computation time when compared to the FE solution.

Active cooling

In this second study, higher rate induction heating was achieved by changing from a 10-AWG coil to a smaller 14-AWG coil to increase the current density. In the induction coil, an RMS current of 33 A and voltage 31.5 V were applied at 49.1 kHz. The chosen parameters are again based on current experiment capabilities. The applied torque again remained constant at 21 N m. To achieve high rate cooling, active methods were modeled; a mixture of 90% water and 10% ethylene glycol was simulated to flow through the tube at a volumetric flow rate of 1.2 gal/min (75 cm^3/s). The thermal effect of the flow was simulated using a forced convection boundary condition in the ODE approach. The convection coefficient h and sink temperature T_∞ of 1400 W/C/m^2 and 24°C, respectively, were found through an iterative parametric study. A more rigorous analysis of these convective mechanisms is beyond the scope of this article. The result of the high-rate actuation study is shown in Figure 7.

The only significant deviations from the FE model occur due to the consideration of latent heat. To further explore the results of the ODE and analytical implementations, the normalized rotation (output rotation angle normalized by the ratio of outer diameter to length ($d_0/(2L)$) developed over time is compared between the three models in Figure 8(a). The FE model, nonlinear ODE solution, and analytical solution in Figure 8(b) generally agree as expected based on the previous calibration of Figure 5. It is known that the effects of induction heating and most especially of active cooling led to substantial spatial gradients in the tube not accounted for by the two reduced-order
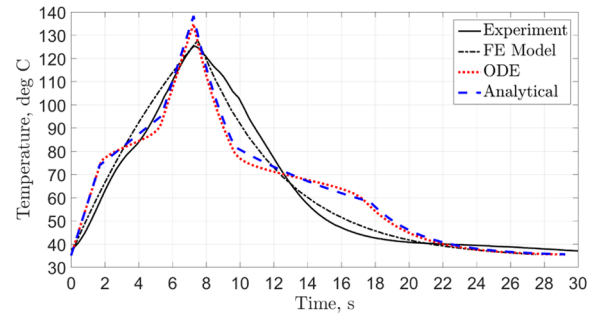

Figure 7. High-rate actuation study results after a parametric study to determine a convection coefficient of 1400 W/C/m^2 and sink temperature of 24°C.
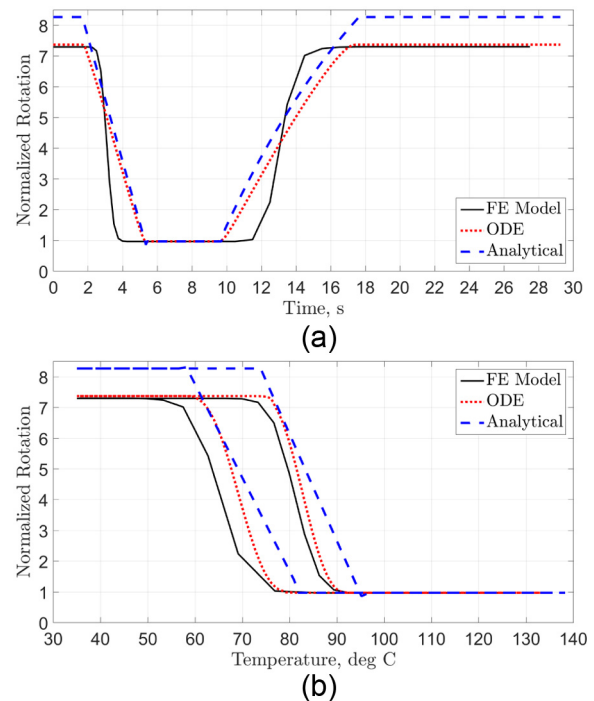

Figure 8. Comparison of normalized rotation developed (a) in time and (b) with temperature between the three models in the SMA tube.

models. Note that the difference in martensite start temperature in between the ODE and analytical model is approximately 3°C and is due to the difference in chosen hardening models. The FE response shown in Figure 5 is smoother than in Figure 8(b) primarily because the heating is accomplished in minutes in the calibration and seconds in the simulation. The FE response could be smoothened by taking smaller time steps, at the cost of greater computation time.

Conclusion

A simplified model for the induction heating of SMA torque tubes has been derived and implemented. The

governing partial differential equations in space and time have been presented and reduced to create two reduced-order engineering models, a nonlinear ODE in time and an analytical solution derived by linearizing the nonlinear ODE. Both derived engineering models have proven to be accurate in predicting the actuation behavior of an SMA torque tube being inductively heated when compared to FEA results. Future work will implement the developed engineering models in optimization frameworks with the goal of improving actuation performance and will utilize these models in control schemes where the reduced computational times are more desirable than the exact behavior.

Acknowledgements

Declaration of conflicting interests

Funding

References

Bekker A and Brinson L (1997) Temperature-induced phase transformation in a shape memory alloy: phase diagram based kinetics approach. *Journal of the Mechanics and Physics of Solids* 45(6): 949–988.

Bertagne C, Hartl D and Cognata T (2015a) Analysis of highly coupled thermal-structural responses in morphing radiative bodies. Available at: https://arc.aiaa.org/doi/abs/10.2514/6.2015-1510

Bertagne C, Sheth R, Hartl D, et al. (2015b) Simulating coupled thermal-mechanical interactions in morphing radiators. In: *SPIE smart structures and materials + nondestructive evaluation and health monitoring*, San Diego, CA, 5 April, pp. 94312F–94312F. International Society for Optics and Photonics.

Bower A (2011) *Applied Mechanics of Solids*. Boca Raton, FL: CRC Press, Taylor & Francis Group.

Boyd J and Lagoudas D (1996) A thermodynamical constitutive model for shape memory materials—Part I: the monolithic shape memory alloy. *International Journal of Plasticity* 12(6): 805–842.

Brinson L and Lammering R (1993) Finite element analysis of the behavior of shape memory alloys and their applications. *International Journal of Solids and Structures* 30(23): 3261–3280.

Coleman B and Noll W (1963) The thermodynamics of elastic materials with heat conduction and viscosity. *Archive for Rational Mechanics and Analysis* 13(1): 167–178.

Coleman B and Noll W (1964) Material symmetry and thermostatic inequalities in finite elastic deformations. *Archive for Rational Mechanics and Analysis* 15(2): 87–111.

Davies J and Simpson P (1979) *Induction Heating Handbook*. London: McGraw-Hill.

Friedman DH, Bieniawski S and Hartl D (2011) Simulation and control design for shape memory alloy torque tubes. In: *ASME 2011 conference on smart materials, adaptive structures and intelligent systems*, Scottsdale, AZ, 18–21 September, pp. 303–313. ASME.

Hartl D and Lagoudas D (2007) Aerospace applications of shape memory alloys. *Proceedings of the Institution of Mechanical Engineers—Part G: Journal of Aerospace Engineering* 221(4): 535–552.

Hartl D and Lagoudas D (2009) Constitutive modeling and structural analysis considering simultaneous phase transformation and plastic yield in shape memory alloys. *Smart Materials and Structures* 18(10): 104017.

Hartl D, Kiefer B and Menzel A (2013) Modeling shape memory alloy single crystalline responses using an anisotropic yield surface. In: *TMS 2013 Supplemental Proceedings*. Hoboken, NJ: John Wiley & Sons, pp. 975–986.

Hartl D, Lagoudas D and Calkins F (2011) Advanced methods for the analysis, design, and optimization of SMA-based aerostructures. *Smart Materials and Structures* 20(9): 094006.

Hartl D, Solomou A, Lagoudas D, et al. (2012) Phenomenological modeling of induced transformation anisotropy in shape memory alloy actuators. In: *SPIE smart structures and materials + nondestructive evaluation and health monitoring*. San Diego, CA, 28 March, pp. 83421M–83421M. International Society for Optics and Photonics.

Herrington J, Hodge L, Stein C, et al. (2015) Development of a twisting wing powered by a shape memory alloy actuator. In: *AIAA SciTech*, Kissimmee, FL, 5–9 January 2015. American Institute of Aeronautics and Astronautics Inc.

Keefe A and Carman G (2000) Thermo-mechanical characterization of shape memory alloy torque tube actuators. *Smart Materials and Structures* 9(5): 665.

Kennedy D, Straub F, Schetky LM, et al. (2004) Development of an SMA actuator for in-flight rotor blade tracking. *Journal of Intelligent Material Systems and Structures* 15(4): 235–248.

Lagoudas D (2008) *Shape Memory Alloys: Modeling and Engineering Applications*. New York: Springer-Verlag.

Lagoudas D, Entchev P, Popov P, et al. (2006) Shape memory alloys, part ii: modeling of polycrystals. *Mechanics of Materials* 38(5): 430–462.

Lagoudas D, Hartl D, Chemisky Y, et al. (2012) Constitutive model for the numerical analysis of phase transformation in polycrystalline shape memory alloys. *International Journal of Plasticity* 32: 155–183.

Lee C and Mavroidis C (2002) Analytical dynamic model and experimental robust and optimal control of shape memory alloy bundle actuators. In: *ASME 2002 international mechanical engineering congress and exposition*, New Orleans, LA, 17–22 September, pp. 491–498. ASME.

Lupi S, Forzan M and Aliferov A (2015) *Induction and Direct Resistance Heating*. Switzerland: Springer.

Mabe J, Fischer B and Hartl D (2013) Characterization and modeling of trained nitinol torsional actuators under reverse bias loads. In: *TMS* 2013 *Supplemental Proceedings*. Hoboken, NJ: John Wiley & Sons, pp. 987–998.

Mabe J, Ruggeri R, Rosenzweig E, et al. (2004) Nitinol performance characterization and rotary actuator design. In: *Smart structures and materials, San Diego, CA*, 16–18 March, pp. 95–109. International Society for Optics and Photonics.

Maugin GA (2013) *Continuum Mechanics of Electromagnetic Solids*, vol 33. Amsterdam, The Netherlands: Elsevier.

Mirzaeifar R, DesRoches R and Yavari A (2010) Exact solutions for pure torsion of shape memory alloy circular bars. *Mechanics of Materials* 42(8): 797–806.

Oehler S (2012) *Developing methods for designing shape memory alloy actuated morphing aerostructures*. Master's Thesis, Texas A&M University, College Station, TX.

Otsuka K and Wayman C (1999) *Shape Memory Materials*. Cambridge: Cambridge University Press.

Patoor E, Lagoudas D, Entchev P, et al. (2006) Shape memory alloys—part 1: general properties and modeling of single crystals. *Mechanics of Materials* 38(5): 391–429.

Prahlad H and Chopra I (2001) Design of a variable twist tilt-rotor blade using shape memory alloy (SMA) actuators. In: *SPIE's 8th Annual International Symposium on Smart Structures and Materials, Newport Beach, CA*, 4–8 March, pp. 46–59. International Society for Optics and Photonics.

Qidwai M, Hartl D and Lagoudas D (2008) Numerical implementation of an SMA thermomechanical constitutive model using return mapping algorithms. In: Lagoudas D (ed.) *Shape Memory Alloys: Modeling and Engineering Applications*. New York: Springer-Verlag, pp. 189–231.

Rudnev V, Loveless D, Cook R, et al. (2002) *Handbook of Induction Heating*. Boca Raton, FL: CRC Press, Taylor & Francis Group.

Sadiku M (2014) *Elements of Electromagnetics*. New York: Oxford University Press.

Sanders B, Crowe R and Garcia E (2004) Defense advanced research projects agency–smart materials and structures demonstration program overview. *Journal of Intelligent Material Systems and Structures* 15(4): 227–233.

Saunders R, Boyd J, Hartl D, et al. (2016) A validated model for induction heating of shape memory alloy actuators. *Smart Materials and Structures* 25(4): 045022.

Saunders R, Herrington J, Hodge L, et al. (2014) Optimization of a composite morphing wing with shape memory alloy torsional actuators. In: *ASME smart materials, adaptive structures and intelligent systems* Newport, Rhode Island, 8–10 September 2014. ASME.

Tabesh M, Liu B, Boyd J, et al. (2013) Analytical solution for the pseudoelastic response of a shape memory alloy thick-walled cylinder under internal pressure. *Smart Materials and Structures* 22(9): 094007.

Takagi T, Luo Y, Suzuki S, et al. (2001) Modeling and numerical simulation on thermomechanical behavior of SMA plates with two-way shape memory effect. *Journal of Intelligent Material Systems and Structures* 12(11): 721–728.

Tiersten H (1990) Energy and momentum in the electromagnetic field. In: Tiersten H (ed.) *A Development of the Equations of Electromagnetism in Material Continua*. Springer, pp. 105–112.

Westgard J (1996) *Electrodynamics a Concise Introduction*. Switzerland: Springer.